Supplementary Materials for

Observation of Nanoscale Skyrmions in $SrIrO_3/SrRuO_3$ Bilayers

Keng-Yuan Meng[1,‡], Adam S. Ahmed[1,‡], Mirko Baćani[2], Andrada-Oana Mandru[2], Xue Zhao[2], Nuria Bagués Salguero[3], Bryan D. Esser[3], Jose Flores[1], David W. McComb[3], Hans J. Hug[2,4] and Fengyuan Yang[1,]*

[1]Department of Physics, The Ohio State University, Columbus, OH, 43210, USA

[2]Empa, Swiss Federal Laboratories for Materials Science and Technology, CH-8600 Dübendorf, Switzerland

[3]Center for Electron Microscopy and Analysis, The Ohio State University, Columbus, OH, 43210, USA

[4]Department of Physics, University of Basel, CH-4056 Basel, Switzerland

Section 1. Sample characterization and basic properties

Figure S1 shows characterization of the quality of a $SrIrO_3$(2 uc)/$SrRuO_3$(10 uc) bilayer on $SrTiO_3$. In Fig. S1a, the SRO(002) X-ray diffraction (XRD) peak shows strong Laue oscillations with the inset showing a narrow XRD rocking curve of 0.05° full-width-at-half-maximum (FWHM). A cross-sectional specimen was made using an FEI Helios NanoLab 600 DualBeam Focused Ion Beam (FIB). In order to protect the 2 uc thick layer of SIO during sample preparation, an additional layer of SRO was deposited on top after the initial growth (TEM specimen only). Ga ion milling and polishing were performed at 30 and 5 kV, respectively, with additional 900 and 500 V Ar ion polishing steps performed in a Fischione 1040 Nanomill to remove any remnant damage from sample preparation. High angle annular dark field (HAADF) scanning transmission electron microscopy (STEM) performed on a probe aberration corrected FEI Titan 80/300 STEM reveals atomically sharp interfaces as shown in Fig. S1b, as indicated by the high contrast between layers. The specimen was imaged with a 20 mrad convergence semi-angle and inner collection angle of approximately 69 mrad.

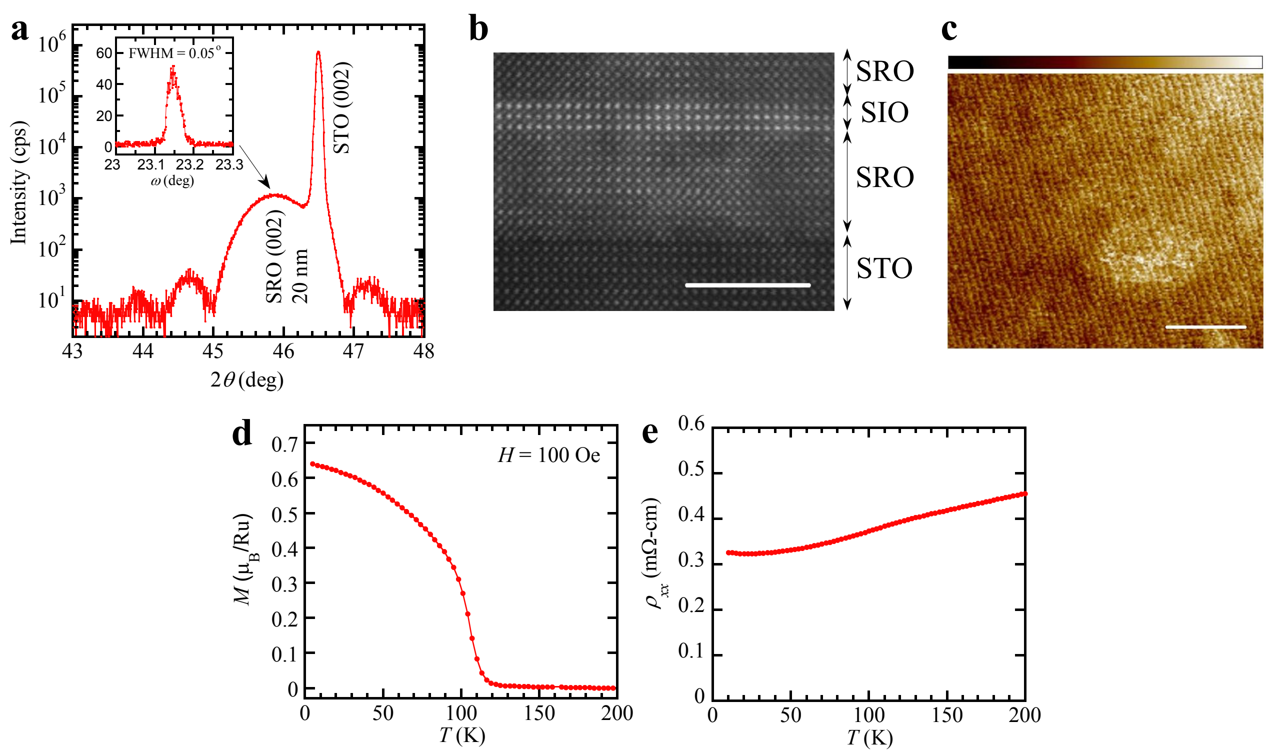

Figure S1. Characterization of $SrIrO_3$(2uc)/$SrRuO_3$(10uc) bilayer quality. **a,** XRD $2\theta/\omega$ scan of a SRO(20 nm) film on STO(001). Inset: rocking curve of the SRO(002) peak. **b,** Cross sectional scanning transmission electron microscopy (STEM) high angle annular dark field image (HAADF). Scale bar: 5 nm

(This specimen has an additional SRO capping layer as a protection layer for TEM sample preparation). **c,** Atomic-force microscopy (AFM) image (length scale bar is 1 μm, color scale bar is from -0.9 nm to +0.8 nm). **d,** Temperature dependence of magnetization of the SIO(2 uc)/SRO(10 uc) bilayer under an applied field of 100 Oe. **e,** Temperature dependence of resistivity at zero field for the bilayer.

All films in this work have been checked by atomic force microscopy (AFM), and they all preserve the flat, step-like surface morphology as shown in Fig. S1c with a root-mean-square (rms) roughness of 0.14 nm. The temperature dependencies of the magnetization (M) and longitudinal resistivity (ρ_{xx}) were measured using a Quantum Design superconducting quantum interference device (SQUID) magnetometer and a physical property measurement system (PPMS), respectively. Figure S1d shows the M-T curves taken with an out-of-plane field of 100 Oe, which reveals a Curie temperatures (T_C) of 112 K, while the temperature dependence of the resistivity shows metallic behavior with a kink around 102 K (Fig. S1e) indicating a magnetic transition.

Section 2. Hall measurement analysis and thickness dependence

The raw data of Hall resistance hysteresis loop is shown in Fig. S2a for a 10 uc BL. The data has a large vertical offset of 6.8 Ω and slightly different slopes in the saturated regime for positive and negative fields. This is a result the longitudinal resistance leaking into the Hall resistance due to finite size and misalignment of the Hall bar electrodes. Through a symmetrization analysis[1], we extract the symmetric component (Fig. S2b) and the antisymmetric component of the raw Hall loop (the antisymmetric components are plotted in the main text). The symmetric component is similar to the magnetoresistivity loop as shown in Fig. S2c, confirming contributions from the longitudinal magnetoresistance. The antisymmetric component, which does not include the longitudinal resistance, is the true Hall resistance loop, which is shown in Figs. 1 and 2a in the main text. Fig. S2d shows anti-symmetrized Hall resistivity at 5, 80 and 90 K. Note the field scale is larger compared to that of Fig. 1 in the main text. For analysis of skyrmion size using $\rho_{\mathrm{TH,\ max}}$

$= PR_o\phi_o n_{sk}$, we extract the ordinary Hall coefficient from Fig. S2d to be R_o= 3.27 nΩ-cm/kOe (1.87 nΩ-cm/kOe) and $\rho_{TH,max}$ value of 0.16 μΩ-cm (0.20 μΩ-cm) at 5 K (90 K). The estimated skyrmion size is 6.3 nm (4.3 nm) at 5 K (90 K).

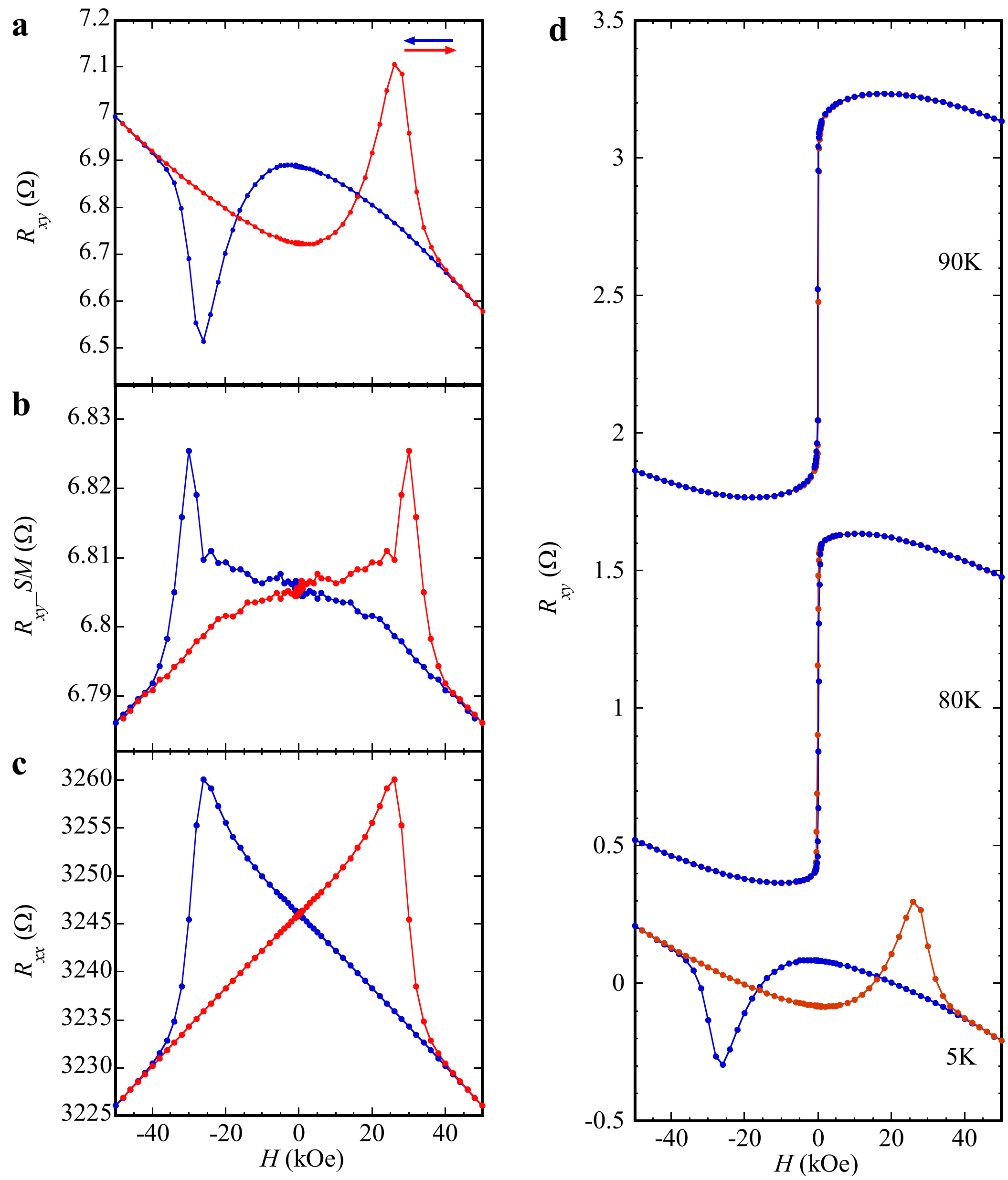

Figure S2. Hall resistivity anti-symmetrization analysis for correction of Hall-bar electrode misalignment for a SIO(2 uc)/SRO(10 uc) bilayer. a, Raw data for Hall resistance hysteresis loop at 5 K, where the slope of -8.72 mΩ/kOe between 40 and 50 kOe is different from the slope of -7.59 mΩ/kOe between -40 and -50 kOe. **b,** Symmetric (SM) part of the Hall loop in (**a**) after anti-symmetrization analysis.

c, Magnetoresistance at 5 K. **d,** Full field view at selected temperatures after anti-symmetrization analysis (80 K and 90 K data are further offset by 1 and 2.5 Ω, respectively, for clarity).

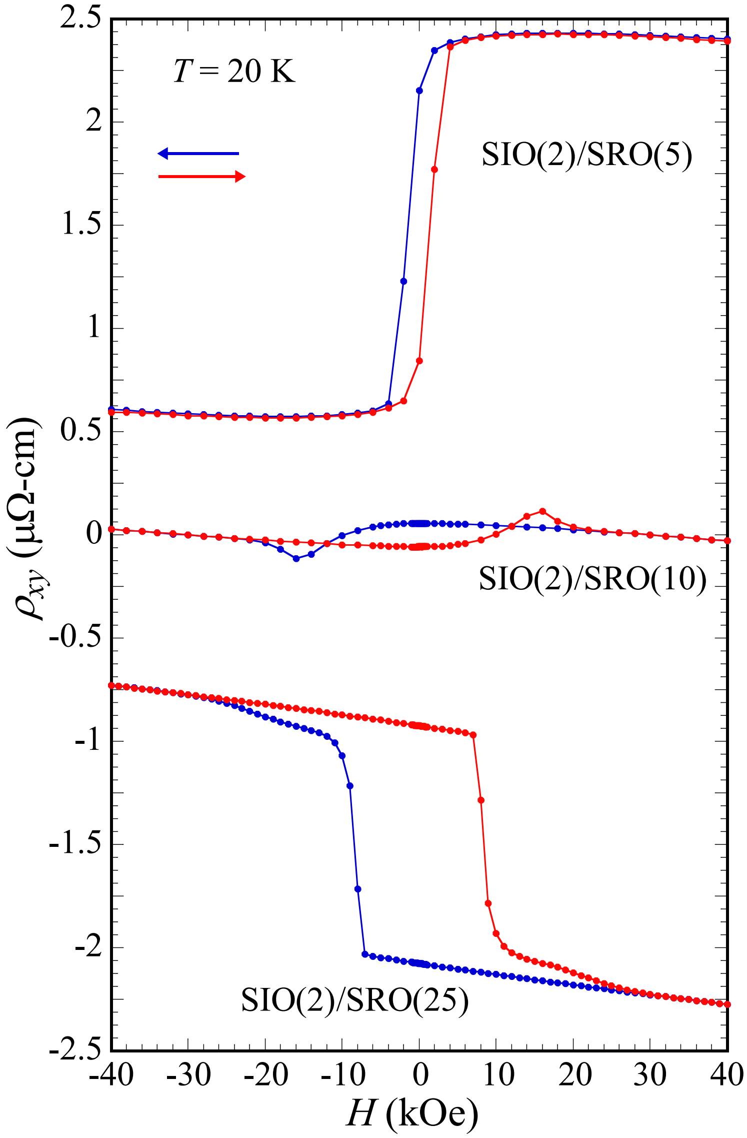

Figure S3. Hall resistivity hysteresis loops of SIO(2 uc)/SRO bilayers with 5, 10, and 25 uc SRO at 20 K, where only the SIO(2 uc)/SRO(10 uc) bilayer shows topological Hall effect.

Figure S3 shows different Hall resistivity hysteresis loops for $SrIrO_3$(2 uc)/$SrRuO_3$ bilayers with various $SrRuO_3$ thicknesses (5, 10, and 25 uc) at 20 K, where only the SIO(2 uc)/SRO(10 uc) bilayer shows distinct topological Hall peaks. The sign of anomalous Hall resistivity changes when the SRO thickness increases to SIO(2 uc)/SRO(25 uc).

Section 3. Magnetic force microscopy

Note on magnetization loops measured by SQUID:

The magnetization loops displayed in main text Fig. 2 have step-like features near zero field. Zero field step-like features have been reported numerous times before in SRO thin films in magnetization hysteresis loops.[2-6] MFM data acquired at 10 K at lower fields do not show any change of the domain structure that can be related to such a low-field step. We thus attribute these near-zero-field steps to a temperature dependent, magnetically soft part of the sample not relevant for the topological Hall effect and the magnetic domain/skyrmion structures analyzed here.

Background Subtraction:

All MFM measurements were performed with the average tip-sample distance kept constant at 10.5 nm using the frequency-modulated capacitive tip-sample distance control described in detailreviously.[7] The tip is scanned parallel to the average slope of the sample surface but does not follow the local sample topography. The local tip-sample distance and with it the local van der Waals force is thus not constant. The measured MFM Δf data hence contains topographical information apart from the signal arising from the magnetic stray field emanating from the sample (Fig. S4a). Note that in contrast to Fig. 3 in the main manuscript, the data shown in Fig. S4a are plotted with a conventional color scale, where a red color denotes a positive frequency shift (repulsive force). Such a contrast is obtained for an antiparallel orientation of the tip and sample magnetization. Hence, red domains have a down magnetization (for an initial up magnetization of the tip).

Apart from the stray field emanating from the up/down domain structure of the SRO layer, two additional sources contribute to the measured Δf contrast:

1. In the measurement mode used here, the tip does not track local topographical features; the local tip-sample distance varies with the topography. Consequently, the van der Waals force varies, giving a non-magnetic, topography-related contribution to the measured Δf signal.
2. The local thickness of the nominally 10 uc thick SRO layer varies by about ±1 uc and connected to it a corresponding variation of the magnetic moment per unit area occurs. The latter then leads to corresponding variation of the stray field and thus frequency shift.

These topographical and magnetic background signals contribute to the measured Δf contrast in addition to the Δf contrast arising from the domain pattern (skyrmions) of the sample.

The stray field of small magnetic features, such as nanometer-sized skyrmions decays rapidly with tip-sample distance such that the Δf signal arising from these objects can become smaller than the topographical or magnetic background contrast, and then becomes difficult to detect. A background subtraction is hence required (Fig. S4): for this, a selected sample area is measured with two opposite magnetization states of the tip (Figs. S4a and S4b). Because at lower temperatures, the domain structure of the sample does not change in a ±100 mT field required to flip the magnetization of the tip, all contrast contributions arise from magnetic fields emanating from the tip magnetization changing sign (compare Figs. S4a and S4b), while the sign of the topography induced van der Waals force remains constant. Figure S4d displays the half-sum of the data sets recorded with up and down magnetization of the tip (Figs. S4a and S4b). Its contrast solely arises from topography-induced van der Waals force gradients. The data taken in saturation (in a field of 7 T) is displayed in Fig. S4c. The contrast contains contributions from the topography and from the stray fields arising from spatial variations of the SRO film thickness. The latter contrast contribution can be separated from the former by a subtraction of the topography induced contrast data displayed in Fig. S4d. The result (a weak granular contrast) is shown in Fig. S4e. To extract the Δf contrast arising from the sample domain structure, the contributions from the topography (Fig. S4d) and from the SRO film thickness variations (Fig. S4e) are subtracted from

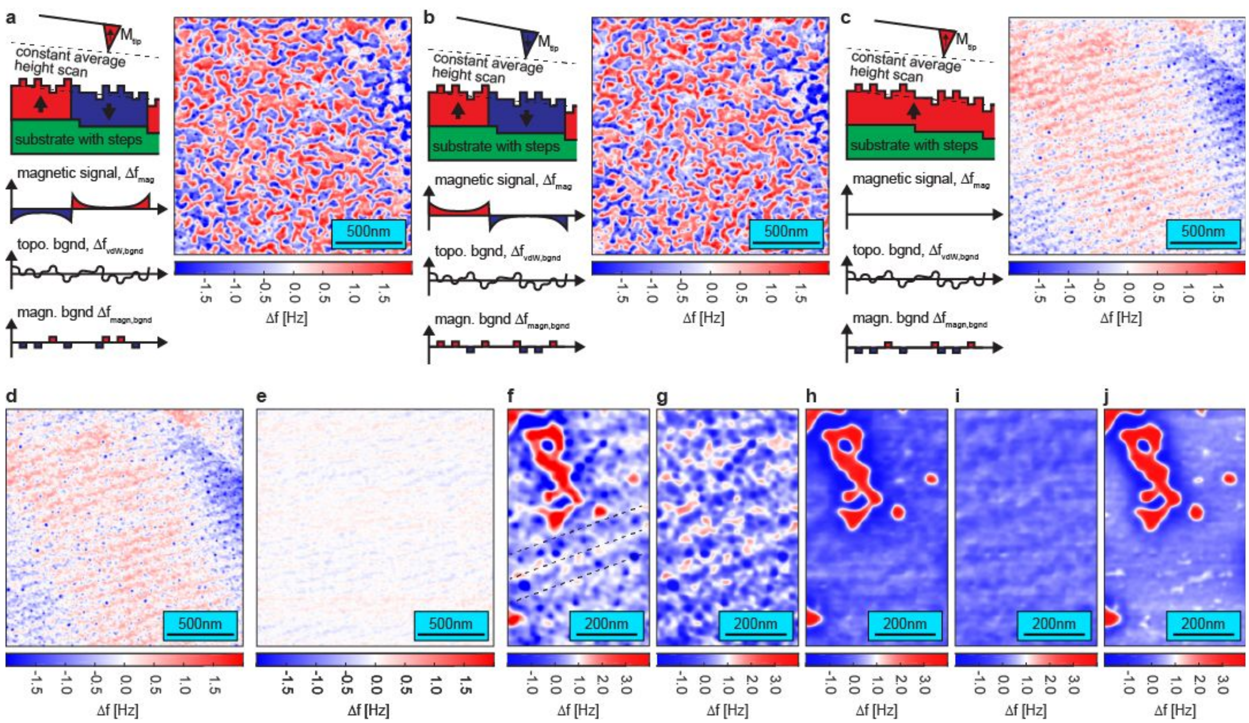

Figure S4: Schematics of the background subtraction. **a**, Left side, upper part: schematics of the SRO film with ±1 uc thickness variation of the nominally 10 uc thick SRO layer contain up/down domains mapped with an MFM tip with an up-magnetization. Left side, lower part: Schematics of the different contributions to the measured total Δf contrast. Right side: MFM results obtained with an up-magnetized MFM tip. **b** corresponds to (**a**) but the MFM tip has a down magnetization. **c** corresponds to (**a**) but the SRO layer is in a saturated state. **d** Half-sum of the Δf data displayed in (**a**) and (**b**). **e**, Magnetic contrast contribution arising from the thickness variations of the SRO layer. The data is obtained from the subtraction of (**d**) from (**c**). **f,** High-magnification image of the raw Δf data. **g,** High-magnification view of topographic background data obtained from (**c**). **h,** Result of the subtraction of **g** from **f**. **i,** High-magnification view of magnetic background data obtained from (**d**). **j,** Result of the subtraction of (**i**) from (**h**). The nano-scale skyrmions are nicely visible in the background subtracted Δf data displayed in (**j**).

the data measured in different fields.

Note that the (magnetic field) contrast arising from the SRO film thickness variation was obtained from the difference of the MFM data obtained in saturation (Fig. S4c) and the frequency shift contrast arising from the spatial variation of the van der Waals force (Fig. S4d). The magnetic background contrast displayed in Fig. S4i is hence obtained for an up orientation of both the tip and sample. The removal of the magnetic background must hence be done domain wise, i.e. by subtraction in the up domains and summation in the down domains.

The importance of the background subtraction process becomes apparent from the data displayed in Figs. S4f-j: Fig. S4f shows the as-measured Δf contrast. A few red domains with a down magnetization are visible inside a larger, blue up domain. The granular white features arranged along the dashed black lines in Fig. S4f, arise from the unit cell steps of the substrate and from the local thickness variation of the SRO layer. A subtraction of the topography-induced Δf contrast (Fig. S4g) leads to a more uniform contrast inside the blue domain (Fig. S4h).

A further subtraction of the magnetic background contrast arising from the SRO thickness variations (Fig. S4i) leads to the Δf data shown in Fig. S4j. The frequency shift displayed in Fig. S4j solely arises from the up/down magnetization structures of the SRO layer. The small skyrmions occurring in the blue domain are now well visible.

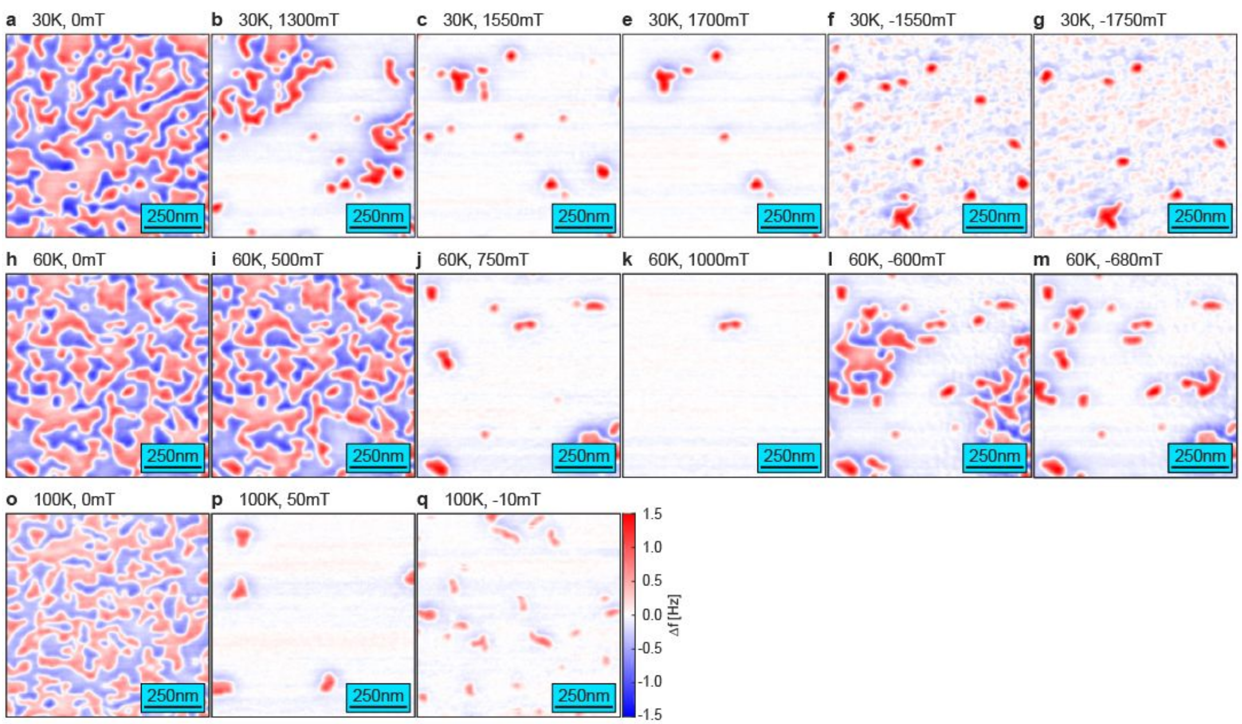

Figure S5. **a-g** MFM data acquired at 30 K in different magnetic fields. **h-m** MFM data acquired at 60 K in different magnetic fields. **o-q** MFM data acquired at 100 K in different magnetic fields.

Temperature Dependent MFM Data:

Figure S5 shows MFM data measured at 30, 60 and 100 K. The field range where a decay of the domain size into skyrmions occurs coincides with that where the peaks of the topological Hall resistivity are observed. Similar to the MFM data obtained at 10 K, the data again show that a high density of nanoscale skyrmions appear at negative nucleation fields after positive saturation. These results together with the topological Hall measurements demonstrate that a large number of nanoscale skyrmions are stabilized in SIO/SRO bilayers over a broad range of temperatures from 5 to at least 100 K.

Calibration of the MFM tip and quantitative data analysis:

The calibration of the MFM tip is performed at 10 K on a $[Co(0.4\ nm)/Pt(1\ nm)]_5$ multilayer sample deposited onto a 5 nm thick Pt seed layer on the native oxide of a Si wafer. The magnetic multilayer was protected with a 2 nm thick top Pt layer against oxidation. The sample was demagnetized with an oscillatory out-of-plane field with a decaying field amplitude. The MFM measurement was performed with a tip-sample distance of 10.5 nm using the frequency modulated capacitive tip-sample distance control mode described reviously.[7] The tip calibration is performed as described in the Supporting Information of Ref. 8. The simulated MFM data displayed in Fig. 4 of the main manuscript is obtained as described in Ref. 8.

References

1. Ahmed, A. S., Rowland, J., Esser, B. D., Dunsiger, S. R., McComb, D. W., Randeria, M. and Kawakami, R. K., "Chiral bobbers and skyrmions in epitaxial FeGe/Si(111) films," *Phys. Rev. Mater.* **2018**, *2*, 041401.
2. Ohuchi, Y., Matsuno, J., Ogawa, N., Kozuka, Y., Uchida, M., Tokura, Y. and Kawasaki, M., "Electric-field control of anomalous and topological Hall effects in oxide bilayer thin films," *Nat. Commun.* **2018**, *9*, 213.
3. Sil, A., Ranjan, R. and Kumar, P. S. A., "Signature of exchange bias and magneto-electric coupling in $BiFeO_3/SrRuO_3$ heterostructure," *J. Magn. Magn. Mater.* **2018**, *448*, 236-242.
4. Grutter, A. J., Wong, F. J., Arenholz, E., Vailionis, A. and Suzuki, Y., "Evidence of high-spin Ru and universal magnetic anisotropy in $SrRuO_3$ thin films," *Phys. Rev. B* **2012**, *85*, 134429.

5. Gao, R., Dong, Y. Q., Xu, H., Zhou, H., Yuan, Y. K., Gopalan, V., Gao, C., Fong, D. D., Chen, Z. H., Luo, Z. L. and Martin, L. W., "Interfacial Octahedral Rotation Mismatch Control of the Symmetry and Properties of $SrRuO_3$," *ACS Appl. Mater. Interfaces* **2016**, *8*, 14871-14878.
6. Ning, X. K., Wang, Z. J. and Zhang, Z. D., "Anisotropy of electrical and magnetic transport properties of epitaxial $SrRuO_3$ thin films," *J. Appl. Phys.* **2015**, *117*, 093907.
7. Zhao, X., Schwenk, J., Mandru, A. O., Penedo, M., Baćani, M., Marioni, M. A. and Hug, H. J., "Magnetic force microscopy with frequency-modulated capacitive tip–sample distance control," *New J. Phys.* **2018**, *20*, 013018.
8. Marioni, M. A., Penedo, M., Baćani, M., Schwenk, J. and Hug, H. J., "Halbach Effect at the Nanoscale from Chiral Spin Textures," *Nano Lett.* **2018**, *18*, 2263-2267.